Quantum Electronics **50** (8) 750–755 (2020)

INTERACTION OF LASER RADIATION WITH MATTER. LASER PLASMA https://doi.org/10.1070/QEL17219

Effect of focused nanosecond laser pulse irradiation on microtribological properties of diamond-like films

V.D. Frolov, P.A. Pivovarov, E.V. Zavedeev, M.L. Shupegin, S.M. Pimenov

Abstract. **We have examined the effect of focused nanosecond laser pulses on the formation and tribological properties of microstructures in the form of a matrix of craters produced in a–C:H:Si:O diamond-like films (DLFs), both undoped and doped with tungsten. The studies are performed by scanning probe microscopy (SPM) using SPM probes of standard design with a tip and probes without a tip (tipless-type probes). A special procedure is developed for assessing the wettability (contact angle) of individual sections of the laser-induced microstructure by the local adhesion force. According to estimates, the material inside the crater becomes softer and more hydrophobic as a result of laser irradiation. This is manifested to the greatest extent in tungsten-doped DLFs, where the crater walls are arranged like terraces formed by 'nanoflakes', i.e. grains of the substance. Scanning of microstructures with a tipless probe in the regime of lateral force microscopy demonstrates a decrease in friction in the crater area.**

Keywords: *nanosecond laser pulses, diamond-like film, microstructure, microtribological properties.*

1. Introduction

It is known that diamond-like carbon films (DLFs) have a solid, chemically inert surface, which makes them attractive for practical applications (in particular, in micromechanical systems [1]).

Technologically, the properties of DLF coatings are determined by a certain ratio between the sp^3 and sp^2 bonds. The high content of sp^3 bonds ensures the hardness of their surface, and vice versa, the low density of sp^3 bonds (and, consequently, the high density of sp^2 bonds) contributes to a decrease in hardness and sliding friction [2–5]. Structural transformations in the DLF surface layers can be obtained by laser treatment [6, 7], which allows selective formation of microstructures on the DLF surface with improved tribological properties (see, for example, work [8–10]).

V.D. Frolov, P.A. Pivovarov, E.V. Zavedeev, S.M. Pimenov Prokhorov General Physics Institute of the Russian Academy of Sciences, ul. Vavilova 38, 119991 Moscow, Russia;
e-mail: p_pivovarov@hotmail.com;
M.L. Shupegin National Research University 'Moscow Power Engineering Institute (MPEI)', ul. Krasnokazarmennaya 14, 111250 Moscow, Russia

Received 9 December 2019, revision received 13 January 2020
Kvantovaya Elektronika **50** (8) 750–755 (2020)
Translated by M.A. Monastyrskiy

One of the priority tasks of tribology is superhydrophobicity of the surface. In the scientific literature, a criterion for achieving hydrophobicity has been developed: The effective contact angle at the water–solid interface, with allowance for the surface roughness, should be at least 150°. Laser structuring of the polytetrafluoroethylene surface made it possible to achieve a high index of superhydrophobicity, i.e. a contact angle of ~170° [11]. As the surface roughness of this material decreases, the effective contact angle also drops, but remains above 90° for a perfectly smooth surface. In other words, only originally hydrophobic materials can exhibit superhydrophobicity due to profiling of the surface of microstructures.

In this work, we use focused nanosecond laser pulses to form surface microstructures in a–C:H:Si:O DLF, both undoped and doped with tungsten. Note that the introduction of silicon into the DLF, on the one hand, causes an increase in the number of sp^3 bonds (i.e. increases the DLF surface's hardness), and, on the other hand, reduces mechanical stresses in the film [12].

Laser-induced microstructures, an array of microcraters in our case, acting as a test object for determining changes in the DLF material properties inside and outside a given laser exposure area and for establishing the reproducibility of this exposure, are studied by means of scanning probe microscopy (SPM) using a specially developed procedure for evaluating the mechanical (degree of rigidity) and microtribological (local adhesion force, degree of wettability) DLF properties before and after laser irradiation. In this regard, one of the important aspects of research is the search for hydrophobic surface areas. Along with this, the friction force on the surface areas of the microstructure outside and inside the laser-affected zone is studied.

2. Experimental

Experiments were performed on both undoped and tungsten-doped a–C:H:Si:O DLFs (hereinafter, DLF 30 and DLF 31, respectively). DLF samples were grown on Si substrates by chemical vapour deposition (CVD) from the gas phase of polyphenylmethylsiloxane (PPMS) vapours [13, 14].

When growing DLFs, deposition of a mixture of PPMS with argon was used. During the technological process, tungsten was introduced using magnetron sputtering of a metal target (the percentage of W in DLF 31 was ~14 at.%) [14]. Deposition conditions and elastic properties of films are described in detail in [15]. In the experiments, DLFs with a thickness of ~2.6 μm (DLF 30) and ~4.3 μm (DLF 31) were used.

The samples were examined using a Ntegra Spectra M scanning probe microscope (SPM). A specific feature of this microscope is the presence of an optical path in its design, which allows irradiating the experimental sample's surface with a laser focused beam, followed by moving the SPM probe into the laser irradiation zone and scanning the SPM probe over a given surface area of the sample. The principal scheme and the result of laser irradiation in the form of an ordered array of craters on the sample surface are shown in Fig. 1.

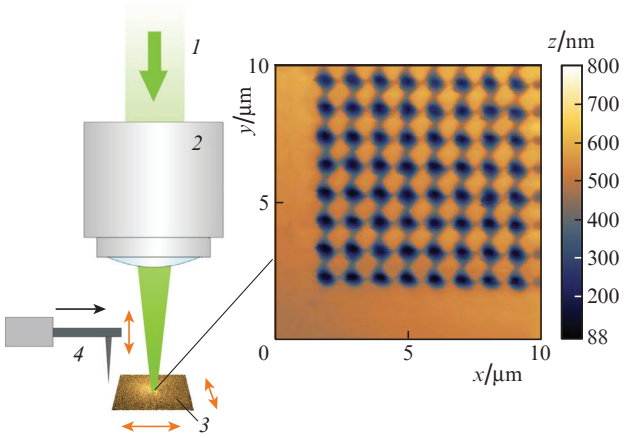

Figure 1. Schematic of the Ntegra Spectra M SPM unit: (*1*) external radiation source (laser); (*2*) SPM optical system; (*3*) sample; (*4*) SPM probe. A typical view of the crater array formation is shown on the right.

In our experiments, the surface of the samples was exposed to radiation of a pulsed Nd:YAG laser focused into a spot with a diameter of ~1 μm (wavelength, 532 nm; pulse duration, 10 ns; pulse energy, 0.7 J cm^{-2}; laser pulse repetition rate, 2.5 kHz; amd exposure time at each point of the matrix, 2 s).

Using laser irradiation, a matrix of 40 × 20 craters was produced on the surface of the samples (linear dimensions of the matrix are 40 × 20 μm). After laser irradiation, the samples were processed in an ultrasonic bath with distilled water for 30 min.

At the initial stage of SPM measurements, the DLF surface relief was recorded in both contact and tapping modes. In the latter case, the phase contrast of the surface was simultaneously recorded. The main part of the experiment was to study the DLF properties by measuring the forces F that occur when the sample contacts the DLF probe. The measure for F is the bend value of the SPM-probe cantilever (recorded on the photodetector in nA). The bend depends on the magnitude and direction of the cantilever tip's movements along the normal to the surface z [the so-called $F(z)$ characteristic]. Measurements were also conducted for a number of test samples [cover glass, indium, highly oriented pyrolytic graphite (HOPG), and Teflon]. The DLF surface was then scanned in the lateral force regime to study the distribution and magnitude of the friction forces. In this case, the measure is the value of the cantilever's torsion angle. Information about the magnitude and distribution of the friction forces on the DLF surface was obtained using special SPM probes without a tip (tipless cantilevers). The cantilever width was ~40 μm. During scanning, the cantilever end was brought into contact with the sample surface. The air humidity in the experiments was RH = 45%–55%.

3. Experimental results and discussion

3.1. Surface relief

As a result of a series of laser impacts on the DLF surface, a matrix of elements was formed, i.e. micropits with a diameter of ~1 μm. Laser effects are reproducible. The matrix fragment for DLF 30 is shown in Fig. 2. In the case of DLF 30, the matrix element is a cone-shaped crater ~300 nm deep with smooth walls (see Fig. 2b).

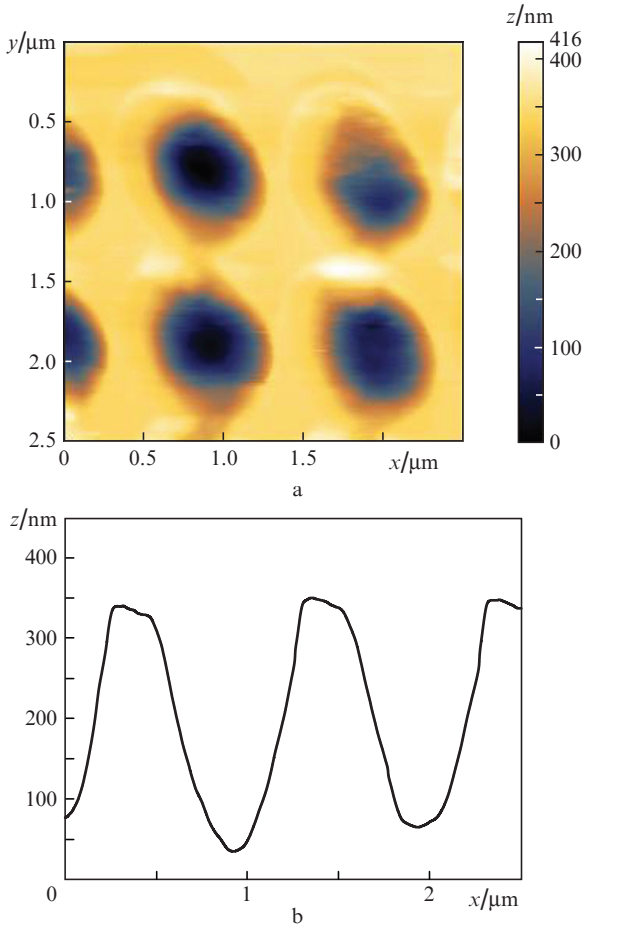

Figure 2. DLF 30 sample: (a) surface microrelief map and (b) surface cross section.

Craters on the DLF 31 surface have a smaller (~150 nm) depth and walls in the form of terraces formed by 'nanoflakes', i.e. grains of the substance with a thickness of ~20–30 nm and lateral dimensions of ~100 nm (Fig. 3). At the crater edge, a redeposition in the form of a collar is observed as a result of the ejection of the material from the crater. The most clearly grained structure of terraces appears on the phase contrast map (Fig. 4).

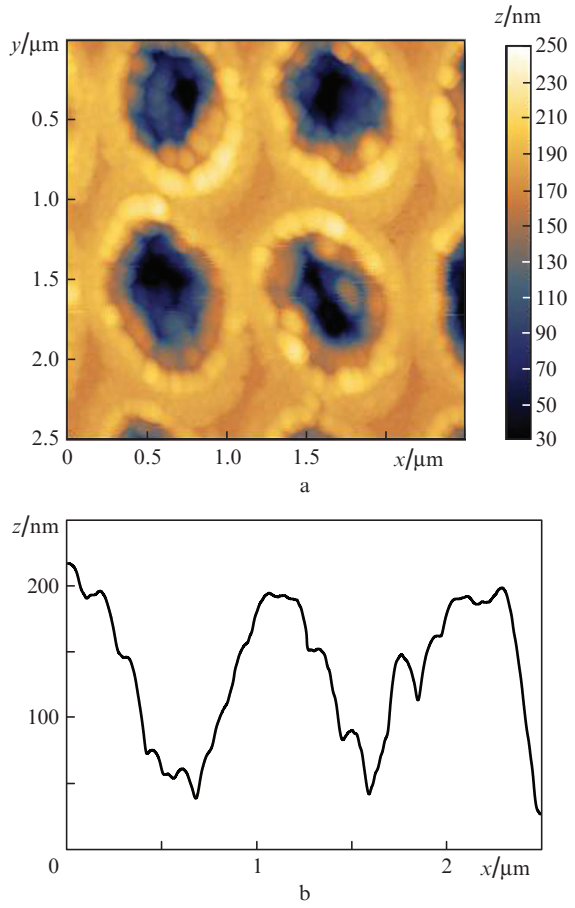

Figure 3. DLF 31 sample: (a) relief map and (b) relief cross section.

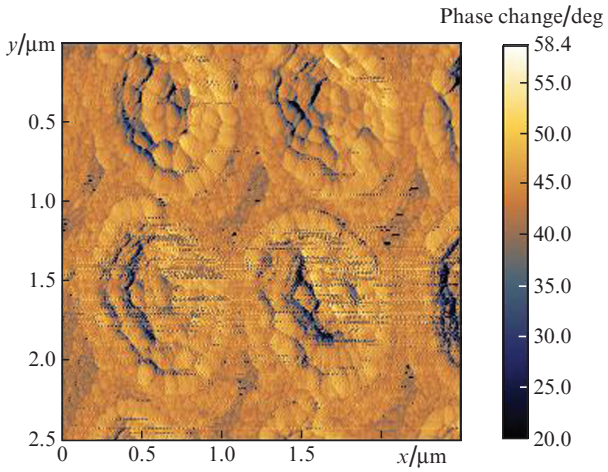

Figure 4. DLF 31 sample: phase contrast map.

The obtained experimental data on the nature of the local destruction of the DLF 31 surface (formation of a nanosized material in the crater zone, formation of terraces) indicate in favour of the crater formation mechanism due to the splitting off of a layer after layer from the film under a series of laser impacts. In the scientific literature, this splitting is referred to manifestation of so-called spallation. Two alternative mechanisms of DLF spallation are considered. The first of them consists in quantised structuring of films due to the appearance of a shock electron wave under conditions of picosecond laser interference [16]. According to the second mechanism, the layer spallation effect is attributed to the action of concentrated mechanical stress caused by differences in the structure evolution processes at different DLF depths under laser irradiation with nanosecond pulses [17, 18]. We consider the second mechanism based on the development of critical stresses in the film as a result of inhomogeneous thermal heating to be more probable.

Note that, in purely external features, namely, the formation of a crater with smooth walls and a relatively small amount of redeposition, the mechanism of crater formation that dominates in DLF 30 differs from that observed in DLF 31 and can be attributed to evaporative ablation [10]. Undoubtedly, the process of the formation of laser-induced craters in the DLF requires further research.

3.2. Characteristic dependences *F*(*z*)

Figure 5 shows the characteristic dependences $F(z)$ recorded when approaching, touching, and pressing the SPM probe into the film, i.e., with decreasing z followed by the probe withdrawal, i.e. when increasing z. For ease of perception, the dependences $F(z)$ are shifted along the abscissa and ordinate axes relative to each other.

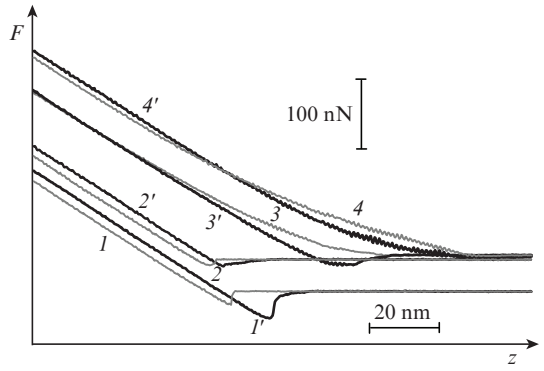

Figure 5. Typical $F(z)$ dependences for the approach (gray curves *1*–*4*) and withdrawal (black curves *1′*–*4′*) of the probe to/from the original surface (*1*, *1′*), the surface between craters outside the laser impact zone (*2*, *2′*), the surface in the laser impact zone (*3*, *3′*, *4*, *4′*).

Summarising the obtained data, we can conditionally distinguish 4 types of $F(z)$ characteristics:

1) on the curves for the original surface, F jumps are visible both when approaching the film surface and when moving away from it (Fig. 5, curves *1* and *1′*);

2) on the curves constructed for most areas of the DLF surface outside the laser impact zone, F jumps are also observable (at a distance of at least 1 μm from the crater boundary) both when the probe is approaching and when the probe is withdrawn, but their amplitude is less than in the case of the original surface;

3) the curves characteristic of the surface areas inside the laser impact zone (craters) and on the crater boundary are distinguished by the fact that F jump disappears when approaching the surface; and

4) on the curves characteristic of certain surface areas inside the craters, there are no F jumps both when approaching the surface and when moving away from it.

The spatial distributions of the 'anomalous' characteristics of $F(z)$ (curves *3* and *4* for DLF 30 and DLF 31) are shown in Fig. 6, where the probe positions when measuring the 'anomalous' curves are marked with white squares. From these distributions, it follows that the main part of the DLF areas with 'anomalous' $F(z)$ characteristics is concentrated inside the crater and also on the crater edge in redeposition areas. The highest spatial density of such areas is observed in DLF 31, while in DLF 30 the proportion of these areas is relatively small. As for curves *2*, their difference from the original curves (curves *1*) can be explained by the incidence of redeposition particles in these places.

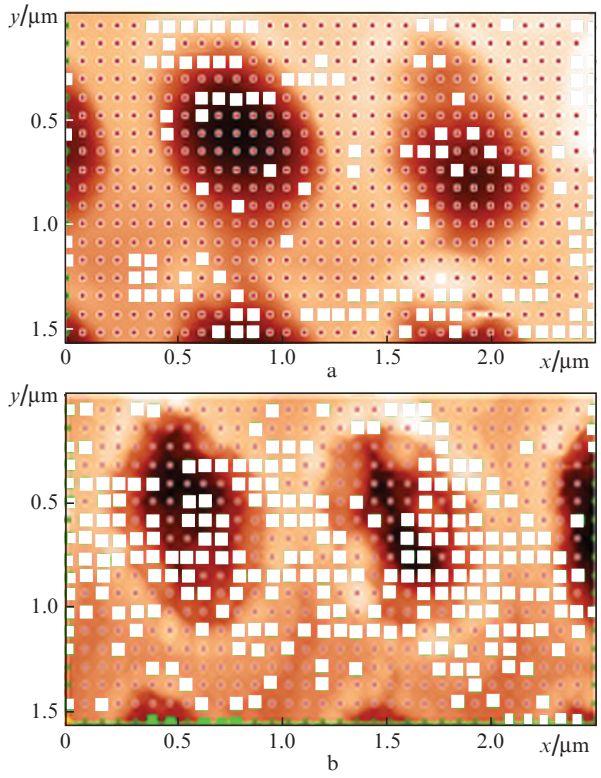

Figure 6. Distribution of 'anomalous' characteristics over the surface: (a) DLF 30 sample and (b) DLF 31 sample.

The process of pressing the SPM-probe tip into the film can be represented as compression of two sequentially connected springs: a cantilever beam and an elastic film material. The slope of the $F_{load}(z)$ dependence when approaching the probe can be expressed as

$$F_{load}/z = (1/k_c + 1/k_s)^{-1}, \quad (1)$$

where k_c is the force constant of the cantilever and k_s is the elastic coefficient of the film.

When probing materials that we further refer to as 'solid', i.e. when $k_s \gg k_c = 3.5$ nN nm^{-1}, the slope of the $F_{load}(z)$ dependence is determined by the cantilever's force constant, i.e. $F_{load}/z \sim k_c = \text{const}z$. In a reverse situation, when probing 'soft' materials, i.e. at $k_s \ll k_c$, we have $F_{load}/z \sim k_s$, and the $F_{load}(z)$ slope depends on the elastic properties of the film and its reactions to the probe pressure.

Let us estimate the approximate critical value of the Young's modulus E_{cr}, i.e. when $k_s \approx k_c$. We use the well-known formula $k = ES/L$ for the elastic coefficient of the material, where E is the Young's modulus of the film material; L is the film thickness; $S = 2\pi R^2$ is the contact area of the cantilever tip with the film; and R is the tip end's radius.

At $R \approx 10$ nm and $L \approx 1$ μm, we have $E_{cr} \approx 5$ GPa. For relatively 'solid' materials ($E > E_{cr}$), the force F_{load} linearly depends on z. For 'soft' materials ($E < E_{cr}$), the $F_{load}(z)$ dependence is nonlinear, which, among other things, is related to the $F(z)$ measurement technique in SPM. Indeed, as follows from the elasticity theory (see, for example, [19]), when the tip is pressed into an elastic half-space (film), the $F_{load}(z)$ slope is expressed (in the approximation of an incompressible sphere) by a nonlinear function of the form

$$F_{load}/z = ER^{1/2}z^{1/2}/(1-\upsilon^2), \quad (2)$$

where υ is Poisson's ratio.

Thus, the form of $F_{load}(z)$ dependence indirectly indicates the degree of the test sample rigidity. Moreover, if the $F_{load}(z)$ dependence is linear, it is possible to calibrate the F values along the ordinate axis. For example, for HOPG, the Young's modulus is $E \approx 17.5$ GPa [20], and $F_{load}(z)$ is linear (Fig. 7). From data on measuring the $F_{load}(z)$ slope for HOPG and the force constant data of the SPM probe, we obtain for 1 nA along the ordinate axis $F = 1.75 \times 10^2$ nN, which was used to normalise other dependences in Fig. 5 and Figs 7, 8.

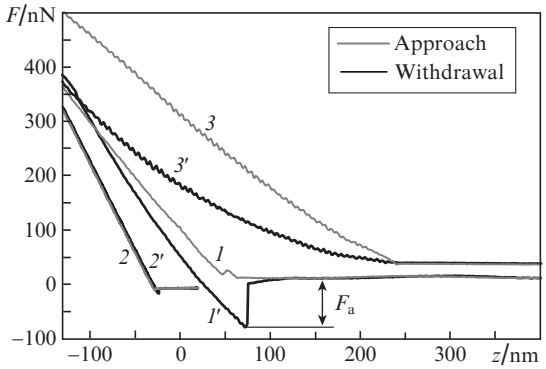

Figure 7. $F(z)$ dependences for the approach/withdrawal: (*1*, *1′*) indium; (*2*, *2′*) graphite; (*3*, *3′*) Teflon.

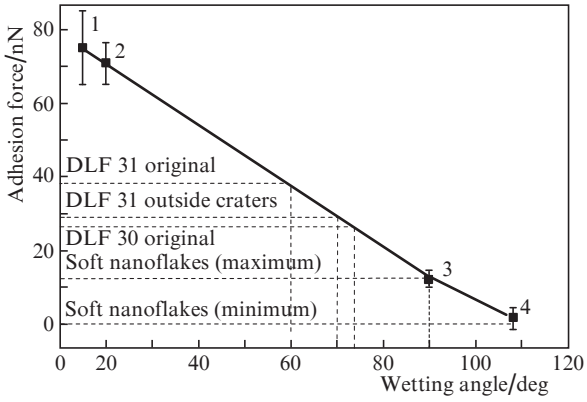

Figure 8. Experimental relationships between the local adhesion force F_a and the wetting angle: 1 = cover glass; 2 = indium; 3 = HOPG; 4 = Teflon.

Note that the original DLF 30 and DLF 31 films also show a linear $F_{load}(z)$ dependence, i.e. they can be attributed to 'solid' materials. The ordinate axis normalisation according to $F_{load}(z)$ data actually coincides with the normalisation established with the use of HOPG. On the contrary, most of the DLF inside craters are characterised by nonlinear $F_{load}(z)$ dependences (see curves *3* and *4* in Fig. 5), which can be interpreted as the reaction of a 'soft' material to the probe pressure. (Note that in the latter case, such a reaction can be caused not only by the internal elastic properties of the modified material, but also by a design effect, i.e. spring-loading of a nanoflake under pressure from the probe).

Experimentally, the assumption that the shape of the curve $F_{load}(z)$ depends on the degree of the test material rigidity is confirmed, along with HOPG measurements, by the results of measuring the $F(z)$ characteristics for indium and Teflon. Indium is a soft material (elasticity modulus is 3 GPa) [21], Teflon is an ultra-soft material (elasticity modulus is 0.4–0.8 GPa) [22]. The results of the $F(z)$ dependence measurements for indium, HOPG, and Teflon are presented in Fig. 7. It can be seen that, in contrast to HOPG, the $F_{load}(z)$ dependence for indium and Teflon is nonlinear with respect to z.

3.3. Local adhesion force, relationship with material wettability

It is known that the jump in $F(z)$ dependence, which occurs when the SPM probe moves away from the sample surface (see, for example, Fig. 7; curve *1′*), indicates the force F_a of water adhesion to the sample surface at a given point on the surface [23]. Below we establish the relationship between this local (microscopic) parameter and the wettability (hydrophilicity/hydrophobicity of the material), the value of which is determined by the edge (contact) angle between water and the sample surface. Thus, in the approximation of a spherical indenter (tip), the relationship between the local adhesion force and the contact angle can be represented, according to calculations [24], as

$$F_a \approx R\sigma_{12}(\cos\theta_1 + \cos\theta_2), \qquad (3)$$

where σ_{12} is the surface tension at the interface of two phases (water–gas); θ_1 is the water–film contact angle; and θ_2 is the water–SPM probe contact angle. From relation (3) it follows that, all other things being equal, the contact angle θ_1 is inversely proportional to the adhesion force F_a.

Due to the design features of the probe microscope, direct measurement of the contact angle in the conditions of our experiment is challenging. Therefore, here we have in mind the establishment of an empirical relationship providing a quantitative assessment of the relations between F_a and θ for these experimental samples within randomly selected areas of their surfaces. The solution to this problem is to construct a calibration curve using the coordinates of points (θ, F_a) obtained as a result of SPM measurements of statistical values of F_a for test samples of certain materials and known tabulated values of the contact angle θ for these materials.

The resulting calibration curve $F_{cal}(\theta)$ is shown in Fig. 8. In our case, we used data on the contact angle θ for cover glass ($\theta \approx 15°$, [25]), indium ($\theta \approx 20°$, [21]), HOPG ($\theta \approx 90°$, [20]), and Teflon ($\theta \approx 110°$, [22]). The procedure for determining the degree of wettability (contact angle θ) for new objects (in our case, DLF 30 and DLF 31) consists in SPM measurement of the adhesion force F_a for a given object and determining the value of the contact angle of wettability using the calibration curve F_{cal} (Fig. 8). It is important that SPM measurements of the test samples and the new object are made under the same conditions, including the relative humidity of the environment, and with the same instrument (SPM probe).

Figure 8 shows the results of F_a measurements for DLFs and their relationship to the contact angle. The highest F_a values for the original DLF surface were recorded for the tungsten-doped DLF 31 film with the corresponding contact angle $\theta \approx 60°$, which means that this film is the most hydrophilic. The wettability of the undoped DLF 30 film is characterised by a large contact angle $\theta \approx 70°$. After laser irradiation, the contact angle on the surface of the DLF 31 film outside the craters increases to $\theta \approx 70°$. Note that these estimated values of θ are in satisfactory agreement with the data $\theta \approx 65° - 70°$, obtained using the drop method for similar DLFs [10]. Inside the craters, the material is characterised by a significantly larger contact angle which amounts to 90° – 110°.

Summing up the above experimental data, we can conclude that as a result of laser impact, the rigidity of the modified DLF material in the crater area decreases and it becomes hydrophobic.

3.4. Friction force

The distributions of lateral forces on the surface of the crater matrix in DLF 31, which contains a large number of areas with 'anomalous' $F(z)$ characteristics, when scanning with a sharp ($R \approx 10$ nm) tip and a tipless-type probe are shown in Fig. 9.

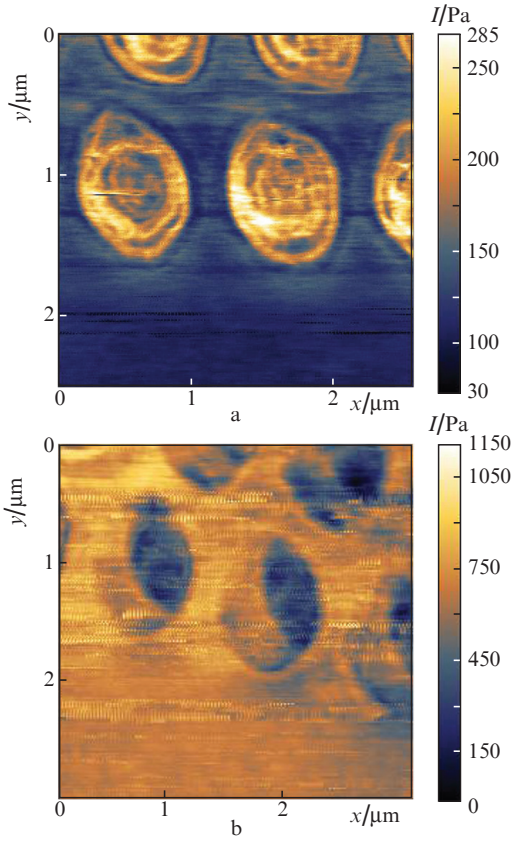

Figure 9. Distribution of lateral forces on the surface of the laser-induced structure in DLF 31: (a) scanning with a sharp tip; (b) scanning with a tipless-type probe.

The resulting friction force on the maps was obtained by subtracting images of lateral forces recorded during forward and reverse scanning of the probe, in order to reduce the contribution of the relief slope to the signal of lateral forces [26].

When scanning with a sharp tip in the laser irradiation zone (craters), an increase in lateral forces and, consequently, friction forces, is observed (see Fig. 9a). As shown in [10], the main reason for an increase in the friction force (in our case, inside and around craters) when scanning with a sharp ($R \approx 10$ nm) tip is the effect of nanoscale roughness, which leads to an increase in the material resistance to the SPM probe's movement along the DLF, including due to the 'plowing' effect.

According to estimates of the details of the map of lateral forces in Fig. 9b, the effective radius of the tipless probe is 100 nm, i.e. an order of magnitude greater than in the case of a 'sharp' tip. When using a tipless probe, the effect of nanoscale roughness on the probe interaction with the sample surface is significantly reduced due to an increase in the effective probe radius. As can be seen from Fig. 9b, an area with a reduced friction force is observed inside the crater, which indicates a decrease in the amount of water adsorbate in the zone of the probe contact with the surface. This, in turn, confirms the assertion that the material inside the crater is hydrophobic.

4. Conclusions

The impact of focused nanosecond pulsed laser radiation on a–C:H:Si:O DLFs leads to the formation of microcraters in the film. In an undoped DLF, craters have smooth walls. In films doped with a metal (tungsten), craters include nanoflakes of the material that are arranged in terraces on the crater walls.

It can be assumed that this is due to laser-induced spallation. Using the results of SPM experiments and a special data processing procedure, we estimated the local adhesion force and wettability of DLFs outside and inside the craters formed. According to our estimates, the DLF material modified by laser irradiation becomes softer and more hydrophobic. This is most pronounced in a tungsten-doped DLF. The use of tipless-type SPM probes significantly reduced the impact of the 'plowing' effect on the friction when the probe moves along the sample surface and revealed a zone of reduced friction inside the craters.

It is important that the process of laser-induced modification of the DLF surface is reproducible (~800-point laser irradiation was performed on the sample). This allows for the formation of a microstructure with dense spatial packing and various configurations (one-dimensional and two-dimensional gratings, concentric grooves, etc.) on the DLF surface.

Noteworthy is the efficiency of the technological method of doping a–C:H:Si:O DLFs with a metal in terms of converting the DLF material from hydrophilic to hydrophobic, which creates prerequisites for the formation of superhydrophobic microstructures (most probable, for micromechanical sliding friction systems). Undoubtedly, the issues of particular practical application of microstructures based on laser-induced a–C:H:Si:O DLFs require further careful study.

Acknowledgements. This work was supported by the Russian Science Foundation (Project No. 15-12-00039).

References

1. Krauss A.R., Auciello O., Gruen D.M., Jayatissa A., Sumant A., Tuceka J., Mancini D.C., Moldovan N., Erdemir A., Ersoy D., Gardos M.N., Busmann H.G., Meyer E.M., Ding M.Q. *Diam. Relat. Mater*., **10**, 1952 (2001).
2. Erdemir A., Donnet C. *J. Phys. D: Appl. Phys.,* **39**, R311 (2006).
3. Wei Q., Narayan J. *Int. Mater. Rev.,* **45**, 133 (2000).
4. Robertson M. *Mater. Sci. Eng. Rep*., **37**, 129 (2002).
5. Dienwiebel M., Verhoeven G., Pradeep N., Frenken J., Heimberg J., Zandbergen H. *Phys. Rev. Lett*., **92** (12), 126101 (2004).
6. Kononenko T.V., Kononenko V.V., Pimenov S.M., Zavedeev E.V., Konov V.I., Romano V., Dumitru G. *Diam. Relat. Mater*., **14**, 1368 (2005).
7. Dumitru G., Romano V., Weber H.P., Pimenov S., Kononenko T., Sentis M., Hermann J., Bruneau S. *Appl. Surf. Sci*., **222**, 226 (2004).
8. Ding Q., Wang L., Hua L., Hu T., Wang Y. *Wear*, **274 – 275**, 43 (2012).
9. Roch T., Klein F., Guenther K., Roch A., Mühl T., Lasagni A. *Mater. Res. Express*, **1**, 035042 (2014).
10. Zavedeev E.V., Jaeggi B., Zuercher J., Neuenschwander B., Zilova O.S., Shupegin M.L., Presniakov M.Yu., Pimenov S.M. *Wear*, **416–417**, 1 (2018).
11. Zhizhchenko A., Kuchmizhak A., Vitrik O., Kulchin Yu., Joudkazis S. *Nanoscale*, **10**, 21414 (2018).
12. Damasceno J.C., Camargo S.S. Jr, Cremona M. *Mat. Res*., **6** (1), 19 (2003).
13. Dorfman V.F. *Thin Solid Films,* **212**, 267 (1992).
14. Shulegin M.L. *Zavodskaya Laboratoriya. Diagnostika Materialov*, **79** (2), 28 (2013).
15. Zavedeev E.V., Zilova O.S., Barinov A.D., Shupegin M.L., Arutyunyan N.R., Jaeggi B., Neuenschwander B., Pimenov S.M. *Diam. Relat. Mater*., **74**, 45 (2017).
16. Kumar K., Lee K.K.C., Li J., Nogami J., Kherani N.P., Herman P.R. *Light: Science & Applications,* **3**, e157 (2014).
17. Ding Q., Wang L., Hu L., Hu T., Wang Y., Zhang Y. *J. Appl. Phys*., **109**, 013501 (2011).
18. Kononenko T.V., Pimenov S.M., Kononenko V.V., Zavedeev E.V., Konov V.I., Dumitru G., Romano V. *Appl. Phys. A*, **79**, 543 (2004).
19. Il'yushkin A.A., Lomakin V.A., Shmakov A.P. *Zadachi i uprazhneniya po mekhanike sploshnoi sredy* (Problems and Exercises in Continuum Mechanics) (Moscow: MSU Publ., 1979).
20. Taherian F., Marcon V., van der Vegt N.F.A. *Langmuir*, **29**, 1457 (2013).
21. Kim J., Schoeller H., Cho J., Park S. *J. Electron. Mater*., **37** (4), 483 (2008).
22. Ghessick J.H., Healey F.H., Zettlemoyer A.C. *J. Phys. Chem*., **60** (10), 1345 (1956).
23. Kaibara Y., Sugata K., Tachiki M., Umezawa H., Kawarada H. *Diam. Relat. Mater*., **12**, 560 (2003).
24. Stifter T., Marti O., Bhushan B. *Phys. Rev. B*, **62**, 13667 (2000).
25. Iglauer S., Salamah A., Sarmadivaleh M., Liu K., Phan C. *Int. J. Greenhouse Gas Control*, **22**, 325 (2014).
26. Ogletree D.F., Carpick R.W., Salmeron M. *Rev. Sci. Instrum*. **67**, 3298 (1996).